Research Square

Preprints are preliminary reports that have not undergone peer review. They should not be considered conclusive, used to inform clinical practice, or referenced by the media as validated information.

Efficient oxygen evolution reaction of FeCoNiWx medium entropy alloy film electrodes for water splitting

Yong Liu
Beihang University
Honghui Zhang
Zhanghonghui@buaa.edu.cn

Beihang University
Yuan Gao
Beihang University
Zhenyu Jiang
Beihang University
Wenjie Zhang
Beihang University
Tianyi Song
Beihang University
Yao Zhang
Beihang University
Yubin Pan
Beihang University
Peishu Yang
Xinyang Normal University
Kaigui Zhu
Beihang University

Research Article

Keywords: Medium entropy alloy film, Oxygen evolution reaction, Tungsten, Overpotential

Posted Date: October 22nd, 2026

DOI: https://doi.org/10.21203/rs.3.rs-10891926/v1

License: This work is licensed under a Creative Commons Attribution 4.0 International License.
Read Full License

Additional Declarations: No competing interests reported.

Efficient oxygen evolution reaction of $FeCoNiW_x$ medium entropy alloy film electrodes for water splitting

Yong Liu [a] [&], Honghui Zhang [a] [&], Yuan Gao [a], Zhenyu Jiang [a], Wenjie Zhang [a], Tianyi Song [a], Yao Zhang [a], Yubin Pan [a], Peishu Yang [b] *, Kaigui Zhu [a] *

[a] School of Physics, Beihang University, Beijing 100191, People's Republic of China
[b] Collaborative Innovation Center of Henan Province for Engery-Saving Building Materials, Xinyang Normal University, No. 237, Nanhu Road, Shihe District, Xinyang City, Henan Province, People's Republic of China

[&] These authors contributed equally to this work and should be considered co-first authors.
* Corresponding Author.

E-mail address: kgzhu@buaa.edu.cn (Kaigui Zhu), yangqimingcqu@163.com (Peishu Yang), zhanghonghui@buaa.edu.cn (Honghui Zhang)

Abstract

Developing efficient oxygen evolution reaction catalysts is pivotal for water splitting. In this study, we fabricated FeCoNiW thin-film electrodes with varying tungsten content via magnetron sputtering, and systematically investigated the regulatory mechanism of tungsten doping on oxygen evolution reaction performance. The Grazing incidence X-ray diffraction analysis shows that the lattice constant obviously increased due to the incorporation of W. The electrodes doped with W exhibit smaller granular size based on morphological characterization. After the linear sweep voltammetry reconstruction, the electrodes develop more nano-flower-like structures. And the optimal FeCoNiW electrode achieves the lowest oxygen evolution reaction overpotential of 264 mV at 10 mA cm^{-2} and a Tafel slope of 59.09 $mVdec^{-1}$. Electron transfer from Fe to Ni/Co/W facilitates the formation of high-valence Fe oxyhydroxides, which enhances the oxygen evolution reaction electrocatalytic activity. First-principles calculations show that the incorporation of tungsten enhances the Ni d-band center, thereby strengthening the binding of intermediates to Ni sites during the OER process and subsequently accelerating the OER kinetics. This work reveals

the critical role of W in FeCoNi based alloy OER catalysts through a compositional engineering strategy, providing new insights for the design of highly efficient and stable electrocatalysts for water splitting.

Keywords: *Medium entropy alloy film; Oxygen evolution reaction; Tungsten; Overpotential*

1. Introduction

With the ever-increasing global energy demand and escalating environmental challenges, the development of sustainable energy conversion and storage technologies has emerged as a critical imperative in contemporary scientific research [1,2]. Electrocatalytic water splitting has emerged as a prominent clean and efficient hydrogen production strategy, attracting substantial research attention due to its capability to harness electricity derived from renewable energy sources such as solar and wind power for driving water electrolysis processes, thereby generating zero-emission "green hydrogen [3–6]. In contrast to conventional hydrogen production via fossil fuel combustion (such as coal, petroleum, natural gas) that yields “gray hydrogen” with substantial carbon emissions, “green hydrogen” demonstrates near-zero carbon footprint during its production process, thereby being recognized as a genuinely clean energy carrier [7]. The electrocatalytic water splitting mechanism comprises two coupled half-reactions: the hydrogen evolution reaction (HER) at the cathode and the oxygen evolution reaction (OER) at the anode [8]. However, the sluggish kinetics of the alkaline condition, which are characterized by its multi-step proton-coupled electron transfer mechanism and inherent high overpotential, constitute the primary bottleneck in the overall water splitting efficiency. Consequently, the rational design of efficient, durable, and cost-effective OER electrocatalysts has emerged as a pivotal research toward achieving large-scale electrocatalytic water splitting for practical applications[9].

Currently, noble metal-based catalysts (such as RuO_2 and IrO_2) are recognized as the most efficient OER catalysts [10–12]. However, their high cost and scarcity have severely hindered large-scale applications [13]. In contrast, low-cost transition metal

alloys (including Fe, Co, Ni, etc.) have attracted significant attention due to their tunable electronic structures and excellent alkaline environment tolerance [14–22]. Nevertheless, conventional alloys often suffer from insufficient active sites and poor electrical conductivity, limiting their practical performance [23]. High entropy alloys (HEAs) and medium entropy alloys (MEAs) can form unique local electronic environments through the synergistic effects of multiple principal elements, thereby simultaneously enhancing catalytic activity and stability[24–28]. FeCoNiCuPd HEA thin film catalyst demonstrated outstanding performance with ultralow overpotential 194 mV for OER at a current density of 10 mA cm^{-2} , for its highly function (FeCoNi) -oxyhydroxide species formed on the film surface [29]. FeCoNi alloys with Mo coordination exhibit a low overpotential with 250 mV at the current density of 10 mA cm^{-2} in alkaline medium and high OER stability at a high current density of 100 mA cm^{-2} [30]. Collectively, these results demonstrate the immense potential of HEAs in advancing OER electrocatalysis. However, the synthesis of HEAs remains inherently complex and energy-intensive, posing significant challenges for scalable production. Yang et al. deposited FeCoNiCrMo thin film with dense nanosheet array structures on the nickle foam by magnetron sputtering [31]. This catalyst has abundant active sites and shows excellent stability and activity in the OER process. This study demonstrates that magnetron sputtering offers a facile fabrication protocol for HEAs, presenting itself as a promising synthetic avenue while concurrently unlocking novel pathways for designing high-performance transition metal-based electrocatalysts. Besides HEAs systems, the MEAs also show very good OER activity and excellent performance. Dai et al. found that the $CoNiFeCu_{0.1}$ MEA electrode exhibits good OER activity and excellent durability due to the unique hierarchical porous structure and optimized compositions [32]. The electrode performance of some medium-entropy alloys can far exceed that of most high-entropy alloys. Park et al. found that by adjusting the proportions of Fe, Co, Ni, and Cr, the overpotential could be reduced to 187 mV [33].

Among various HEAs and MEAs systems, FeCoNi-based alloys have garnered significant research interest owing to their unique electron correlation effects and

surface reconstruction behavior under electrochemical polarization, which synergistically enhance both charge transfer kinetics and thermodynamic stability [34–36]. Three transition metals (Fe, Co, Ni) are widely employed as electrocatalysts due to their excellent catalytic and stability in alkaline media [37]. Crucially, the incorporation of 5d transition metal W induces lattice strain-mediated d-band center upshift, which optimizes oxygen intermediate adsorption/desorption energy, thereby synergistically enhancing overall catalytic performance. This phenomenon originates from the extended radial distribution of 5d orbitals compared to their 3d counterparts, which facilitates stronger interatomic hybridization with adjacent ligand orbitals [38–40]. Consequently, the electron bandwidth in 5d transition metals substantially exceeds that in 3d metals , enabling broader tunability of electronic structure through d-band center modulation [41]. In addition, 5d metals possess additional orbital degrees of freedom to modulate the electronic band structure and the adsorption/desorption energies of intermediates. The high-valent 5d metal W has been shown to effectively tune the electronic structure of catalysts, thereby optimizing the adsorption/desorption behavior of oxygen intermediates and extending catalyst durability. For example, incorporating W into FeCoNi alloys enhances their OER performance through synergistic electronic coupling effects among Fe, Co, Ni, and W atoms. Ye et al. demonstrated that incorporating W into FeCoNi-based alloys induces changes in the electronic structure of the FeCoNi alloy through 3d-5d orbital hybridization, increases the catalyst's specific surface area and exhibits superior performance [42]. The enhanced overall activity of W-doped FeCoNiMo systems derived from d-band center upshifting toward Fermi level, thereby increasing the adsorption of active intermediates[40]. The d^0 W^{6+} atoms with low-spin states possess more outermost empty orbitals, leading to increased adsorption of water and OH^- groups on the exposed W sites of $Ni(OH)_2$ nanosheets. Density functional theory calculations confirm that both O radicals and O-O coupling occur at the same W^{6+} site [43]. Zhang et al. demonstrated that NiFeCoCrW HEAs enable multi-path electron synergism to activate lattice oxygen oxidation mechanisms (LOM) for enhanced oxygen evolution. By constructing a $NiFeCoCrW_{0.2}$ HEA, they achieved a low

overpotential of 220 mV at 10 mA cm^{-2} and exceptional stability, attributed to Ni-Co dual-site coupling and W-induced electronic modulation [44]. However, systematic research on the influence of different W contents in $FeCoNiW_x$ on their OER performance is still lacking. Therefore, this study aims to fabricate efficient $FeCoNiW_x$ medium entropy alloy thin-film electrodes via magnetron sputtering and systematically investigate the effects of varying W contents on the OER performance and its underlying mechanisms.

In this paper，$FeCoNiW_x$ thin films with different W contents were prepared on nickle foam substrate via magnetron sputtering and the effects of varying W contents on the OER performance in alkaline water were systematically investigated. And we compared of surface morphology and microstructure, as well as the morphological changes after linear sweep voltammetry (LSV) reconstruction. Additionally, we investigated the internal charge transfer and mechanisms by X-ray photoelectron spectroscopy (XPS), providing effective evidence for W's enhancement of the performance of MEAs thin-film electrodes.

2. Experimental

2.1. Material

Equiatomic ratio FeCoNi target (99.9%) with a size of D60×4 mm was customized by Changsha Xinkang New Materials Co., Ltd. The W target (99.9%) with a size of 10 ×10 ×1 mm was produced by Advanced Technology and Materials cooperation using powder metallurgy. Potassium hydroxide (KOHAR) was provided by Aladdin Company. Deionized water was purchased from Zhejiang Nandai Industrial Co., Ltd. Nickel foam was provided by Guangjiayuan New Material Co., Ltd. Ethanol (AR), acetone (AR) and hydrochloric acid were all provided by Modern Oriental (Beijing) Technology Development Co., Ltd.

2.2. Fabrication of FeCoNiWx film electrodes

The 10 mm ×18 mm nickel foams used as substrates were treated in 1 mol/L hydrochloric acid, acetone, ethanol and deionized water for 10 minutes respectively. The working mode of magnetron sputtering is direct current (DC) sputtering. The deposition parameters are as follows: background vacuum is 8×10^{-4} Pa, power supply was 100 W, current was 435 mA, voltage was 230 V, deposition pressure was 1 Pa and deposition time was 60 min. The fabrication process of $FeCoNiW_x$ film electrodes were described (Fig. 1(a)). A series of $FeCoNiW_x$ thin films were prepared by magnetron sputtering on nickel foam substrates for about 60 minutes. By regulating the number of W targets (0, 2, 4, 6, 7) for co-sputtering on the FeCoNi target, the corresponding $FeCoNiW_x$ electrodes were named W0，W2，W4，W6, and W7 respectively. After performing eight LSV cycles, the W0-W7 electrodes were respectively named as LSV-W0, LSV-W2, LSV-W4, LSV-W6, and LSV-W7 electrodes.

2.3. Electrochemical testing

The electrochemical performance of the prepared electrodes was tested using a standard three-electrode system (working electrode: prepared sample, counter electrode: graphite electrode, reference electrode: Hg / HgO) in a CHI600E electrochemical workstation, with the testing medium being 1 mol/L KOH solution. The electrocatalytic activity of the samples can be evaluated by electrochemical surface area (ECSA) which is in direct proportion to C_{dl} and ECSA can be derived from the formula: ECSA = C_{dl}/Cs, and Cs is specific capacitance [45]. The values of C_{dl} were calculated by formula: C_{dl} =$C_{dl} = \frac{(j_a - j_c)/2}{v}$. For this formula, j_a is anodic current and j_c is cathodic current obtained from CV and the scanning potential range is from 1.124 to 1.224 vs.RHE (non-faradaic region). Additionally, v is scan rate of CV (70 mV/s, 80 mV/s, 90 mV/s, 100 mV/s and 120 mV/s). The electrocatalytic OER

stability was evaluated at 10 mA/cm^2 for 12h through chronopotentiometry. LSV was performed at a scan rate of 5 mV/s (scanning window:1.1-1.7V vs.RHE). Chronopotentiometric stability evaluation was conducted at 10 mA cm^{-2} for about 12 h. All potentials were converted to the reversible hydrogen electrode (RHE) scale using the equation:$E_{RHE} = E_{Hg/HgO} + E^{\theta}_{Hg/HgO} + 0.0591pH$.Where E_{RHE} is the potential relative to the reversible hydrogen electrode, $E_{Hg/HgO}$ is the measured potential of work electrode versus Hg/HgO electrode, $E^{\theta}_{Hg/HgO}$:the potential of Hg/HgO electrode which is relative to standard hydrogen electrode.

2.4. Materials Characterization

Grazing incidence X-ray diffraction (GIXRD) patterns were collected on a D8 ADVANCE (Bruker, Beijing, China) using a Cu target with a grazing incidence angle of 1° to characterize the crystal structures. The morphology and the element mapping of films were investigated by scanning electron microscopy (FESEM, S4800, Hitachi, Japan) and electron energy dispersive X-ray spectroscopy (EDS, Hitachi, Japan). The XPS was obtained by Thermo Fisher ESCALAB 250Xi to characterize surface states.

2.5. First-principles calculation

Unit cells with the (100) crystallographic plane of FeCoNi and FeCoNiW serving as the exposed surface were constructed. Structural optimization and electronic structure calculations were performed using density functional theory (DFT) as implemented in the Vienna Ab initio Simulation Package (VASP) code. The exchange-correlation interactions were described by the generalized gradient approximation (GGA) [46] paired with the Perdew–Burke–Ernzerhof(PBE) functional [47]. Electron wavefunctions were expanded via plane waves with a cutoff energy of 500 eV. During structural relaxation, the energy convergence tolerance per atom was set to 10^{-5} eV for both systems. The vacuum layer thickness was set to ~15 Å, which

is sufficient to eliminate spurious interactions between periodically replicated slabs caused by the periodic boundary conditions, thereby avoiding interference with the surface properties during adsorption. The density of states (DOS) of FeCoNi and FeCoNiW, as well as the projected density of states (PDOS) of each element, have been calculated and analyzed.

3. Results and discussion

GIXRD analysis (Fig.1(b)) revealed that the W0 sample without W doping exhibited two characteristic diffraction peaks at 44.5° and 51.9°, corresponding to the face-centered cubic (FCC) structure of pure Ni (JCPDS No. 04-0850), respectively. This confirms that it has an FCC phase similar to pure nickel. When W was incorporated into the FeCoNi system in an equimolar ratio to form the W2 electrode, the diffraction peak at 51.9° corresponding to the (200) plane disappeared, while the (111) peak remained, still indicating an FCC structure. The W4 electrode had the same FCC structure as W2. With the incorporation of W, the peak positions in the XRD pattern move toward decreasing 2θ◦. These phenomena can be explained based on the crystal plane-spacing formula and Bragg's equation,

$$d = \frac{a}{\sqrt{h^2 + k^2 + l^2}} \tag{1}$$

$$2d_{hkl} \sin\theta = n\lambda \tag{2}$$

Here, d_{hkl} represents the crystal plane spacing of the alloy sample, a represents the lattice constant of the alloy sample, (hkl) represents the crystal plane index, θ denotes the diffraction angle, n denotes the diffraction order, and λ denotes the X-ray wavelength. when the lattice constant increases, the crystal plane spacing increases and the diffraction angle decreases. Therefore, the lattice expansion caused by the addition of W moves the peak position of the $FeCoNiW_x$ along decreasing 2θ°.

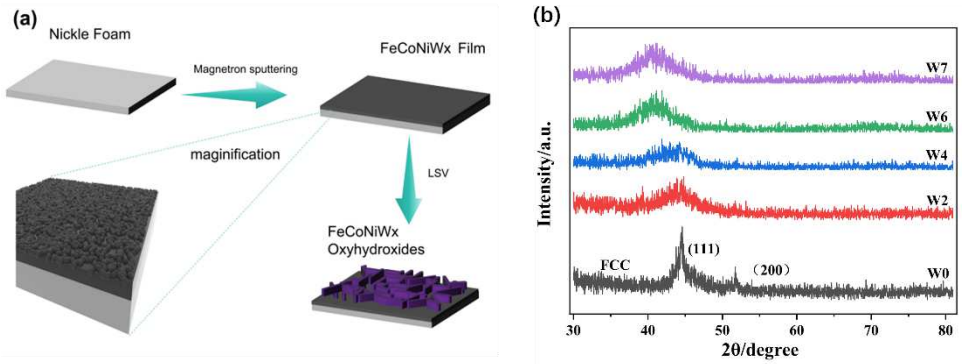

Figure 1. (a) Schematic diagram of the fabrication process of FeCoNiW film electrodes; (b) GIXRD of W0、W2、W4、W6、W7.

Table 1 The atomic percentage of FeCoNiW films with different W content.

Number of targets W	Fe	Co	Ni	W
0	22.08	28.40	49.51	0
2	17.27	21.80	39.70	21.23
4	10.55	12.38	44.86	32.21
6	5.07	6.96	54.32	33.66
7	6.46	7.93	36.17	49.44

Table 1 indicates the atomic percentages of elements in FeCoNiW films with different W contents. Among them, the contents of Fe and Co elements (excluding the base element Ni) are nearly equimolar. The W content in the film increases proportionally with the number of W targets. Fig.2(a)-(e) presents the SEM images and mapping analysis results of FeCoNiW films with different W contents. Fig.2(f) is an enlarge view of Fig.2(e). From the SEM images Fig. 2(a), it can be observed that the surface of the undoped FeCoNi film has very few granular structures. With the incorporation of W atoms, the number of surface granular structures in the equiatomic FeCoNiW film gradually increases, and the catalytic performance improves accordingly. When the ratio of Fe:Co:Ni:W is approximately 1:1:1:3, the surface of the film is covered with granular structures and the catalytic performance is

significantly enhanced. When the ratio is approximately 1:1:1:5, the film exhibits the highest number of particles per unit area with the smallest particle size, leading to the optimal catalytic performance. However, when the ratio reaches approximately 1:1:1:6, the catalytic performance declines. Based on this, the potential optimal doping ratio is determined to be Fe:Co:Ni:W approximately 1:1:1:5, meaning that W6 is the electrode with the best catalytic performance. According to the morphological analysis, a higher number of particles per unit area with smaller particle size on the film surface results in a larger specific surface area. This allows for more sufficient contact with the KOH electrolyte during the subsequent OER reaction, generating more active oxygen-containing species per unit time, thereby endowing the film electrode with a lower oxygen evolution overpotential. The EDS elemental mapping of FeCoNiW for W6 is shown in Fig.2(g).

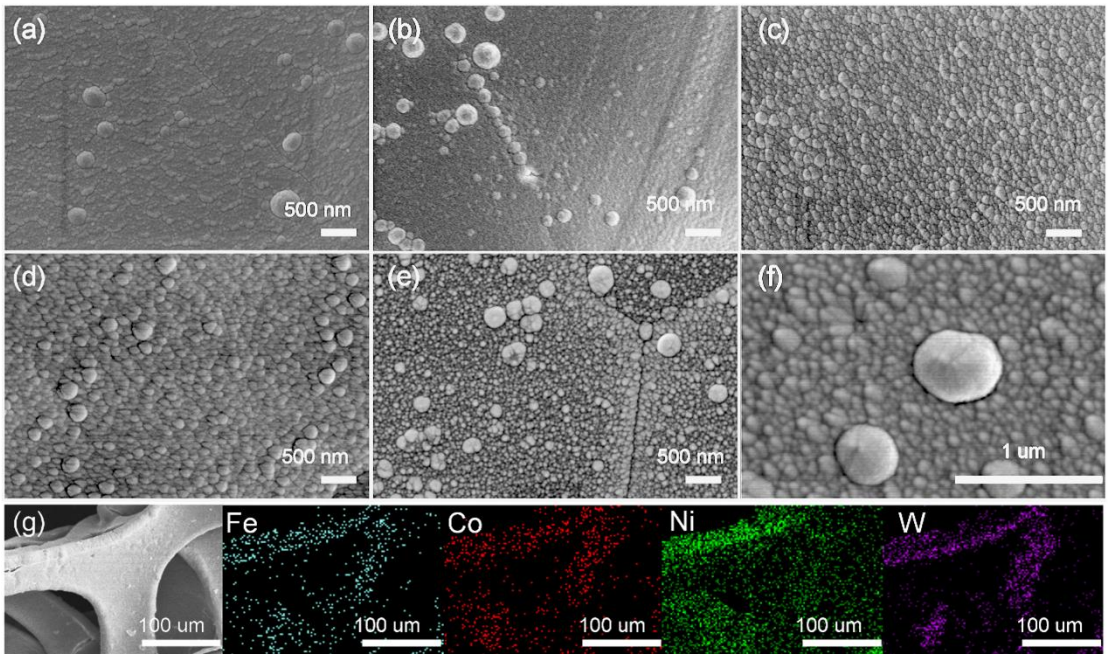

Figure 2. (a)-(e) SEM image in W0, W2, W4, W7, W6; (f) Enlarge view of Fig. (e); (g) EDS elements mapping of Fe/Co/Ni/W in W6.

Fig.3. (a)-(c) show the surface morphology evolution of W6, W7 and W0 thin-film electrodes after 8 cycles of LSV. The surface of the undoped W0 electrode exhibits a sparse nano-flower-like structure (about 600 nm in diameter), while the

surface of the W6 electrode features a uniformly distributed porous nano-flower-like structure (Fig.3(a)). The characteristic size is reduced to 200-300 nm, which promotes the growth of specific surface area. In general, catalysts exhibiting high mass activity often possess smaller particle sizes. This is attributed to the fact that their surface atoms constitute a higher proportion of the total atoms per unit mass and contain a greater number of electrocatalytic active sites [45,48,49]. However, the excessively doped W7 electrode may suffer from pore blockage caused by excessive growth of nano-flower-like structures, leading to mass transfer limitation and performance degradation.

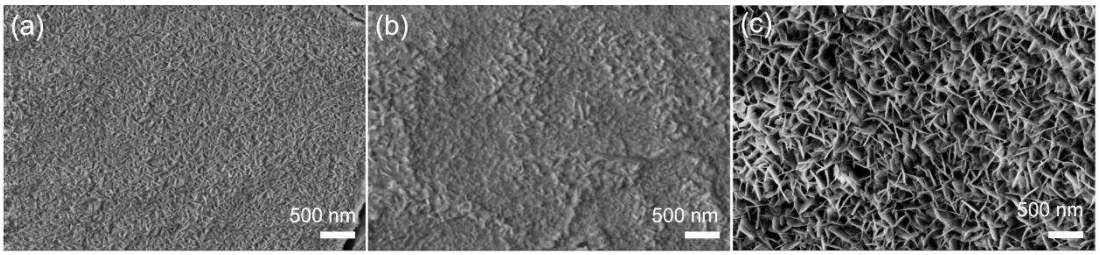

Figure. 3. (a)-(c) SEM images of LSV-W6、LSV-W7、LSV-W0

To elucidate the chemical state evolution of constituent elements in FeCoNiW films during OER, we conducted XPS on W6 samples before and after LSV reconstruction. All XPS peaks were calibrated using the C-C bond at 284.8 eV. As shown in Fig.5(a), the characteristic peaks of six elements C 1s, O 1s, Fe 2p, Co 2p, Ni 2p, and W 4f can be detected in the full spectrum before and after LSV reconstruction. The high-resolution XPS spectra of Fe 2p, Co 2p, Ni 2p, W 4f, and O 1s are presented in Fig.4(b)-(f). The high-resolution XPS 2p spectra for Fe, Co, and Ni in W6 (Fig. 4(b)–(d)) show two main peaks per element: $2p_{3/2}$ and $2p_{1/2}$ before and after LSV reconstruction. These two main peaks can be regarded as the convolution of several binding energy peaks belonging to valence states of 0, +2, +3 or +4 and their satellite peaks[42]. The binding energies of the $2p_{3/2}$ XPS peaks for the oxidation states of Fe/Co/Ni/W on the surface of W6 are 711.51 eV, 782.13 eV ,856.32 eV and 35.39 eV, respectively. And those for LSV-W6 are 711.71 eV, 780.79 eV, 855.99 eV

and 35.09 eV, respectively[30,50,51]. Compared with W6, the binding energies of Co, Ni and W in LSV-W6 shift to lower binding energies by 1.34 eV, 0.33 eV and 0.30 eV, respectively, while the binding energy position of Fe shifts to a higher binding energy by 0.2 eV. This indicates that electrons in the Fe element are transferred to the Ni, Co and W elements. Such electron transfer is favorable for generating high-valence Fe species, namely iron hydroxides or oxyhydroxides, thereby may improve the OER electrocatalytic performance[20,52–54]. In Fig. 4(e), the element W has two main peaks located at 35.4 eV, 37.3 eV and 31.15 eV, 37.3 eV are the convolution of binding energy peaks of W^{6+} $4f_{5/2}$, W^{6+} $4f_{7/2}$ and W^{0} $4f_{5/2}$, W^{0} $4f_{7/2}$, respectively [55]. After LSV reconstruction, the W element shows only one main peak, corresponding to the overlap of the $W6^{+}$ $4f_{5/2}$ and $4f_{7/2}$. This suggests that W has been largely oxidized after LSV reconstruction. Fig.4(f) presents the high-resolution XPS spectra of O 1s for W6 and LSV-W6, which can be deconvoluted into three peaks assignable to surface-adsorbed water (M-H_2O), oxygen vacancies(M-OH), and lattice oxygen(M-O/M-OOH), respectively[56]. The presence of lattice oxygen and oxygen vacancies facilitates the formation of active oxide/hydroxide phases during electrochemical oxidation[57]. Compared to the M-H_2O XPS peak in sample W6, the M-H_2O peak area of the LSV-W6 sample shows no significant difference, whereas the M-OH peak area shows a marked increase. This indicates that a substantial amount of hydroxide/oxyhydroxide species form on the surface of the film during the LSV process, which is consistent with prior SEM observations of newly formed surface phases. These generated hydroxide/oxyhydroxide species contribute to the improved electrocatalytic OER performance.

From another perspective, an initial chemical state analysis was performed on the W0 and W6 electrodes. Fig. 4(g)-(i) show that the binding energies of the $2p_{3/2}$ XPS peaks for the oxidation states of Fe/Co/Ni on the surface of W0 were 710.92 eV, 781.07 eV, and 854.35 eV, respectively. Compared with W0, the binding energies of Fe, Co, and Ni in W6 shifted toward higher binding energies by 0.59 eV, 1.06 eV, and 1.97 eV, respectively. This demonstrates that the doping of the W element leads to the transfer of electrons on the Fe, Co and Ni surfaces and causing a positive shift in the

binding energies of the Fe, Co and Ni elements[30,42]. Additionally, W^{6+} also has a strong electron-withdrawing effect. Outer-shell electron-rich elements such as Mo, Mn, and W, when doped into FeCoNi-based alloys, tend to donate abundant electrons to Fe, Co, and Ni. However, after LSV reconstruction, the high-valence oxidized states of Mo, Mn, and W exhibit stronger electron-withdrawing effects, which instead promote the formation of high-valent active Fe, Co, and Ni species(hydroxide/oxyhydroxide), thereby enhancing the OER rate[42,58,59].

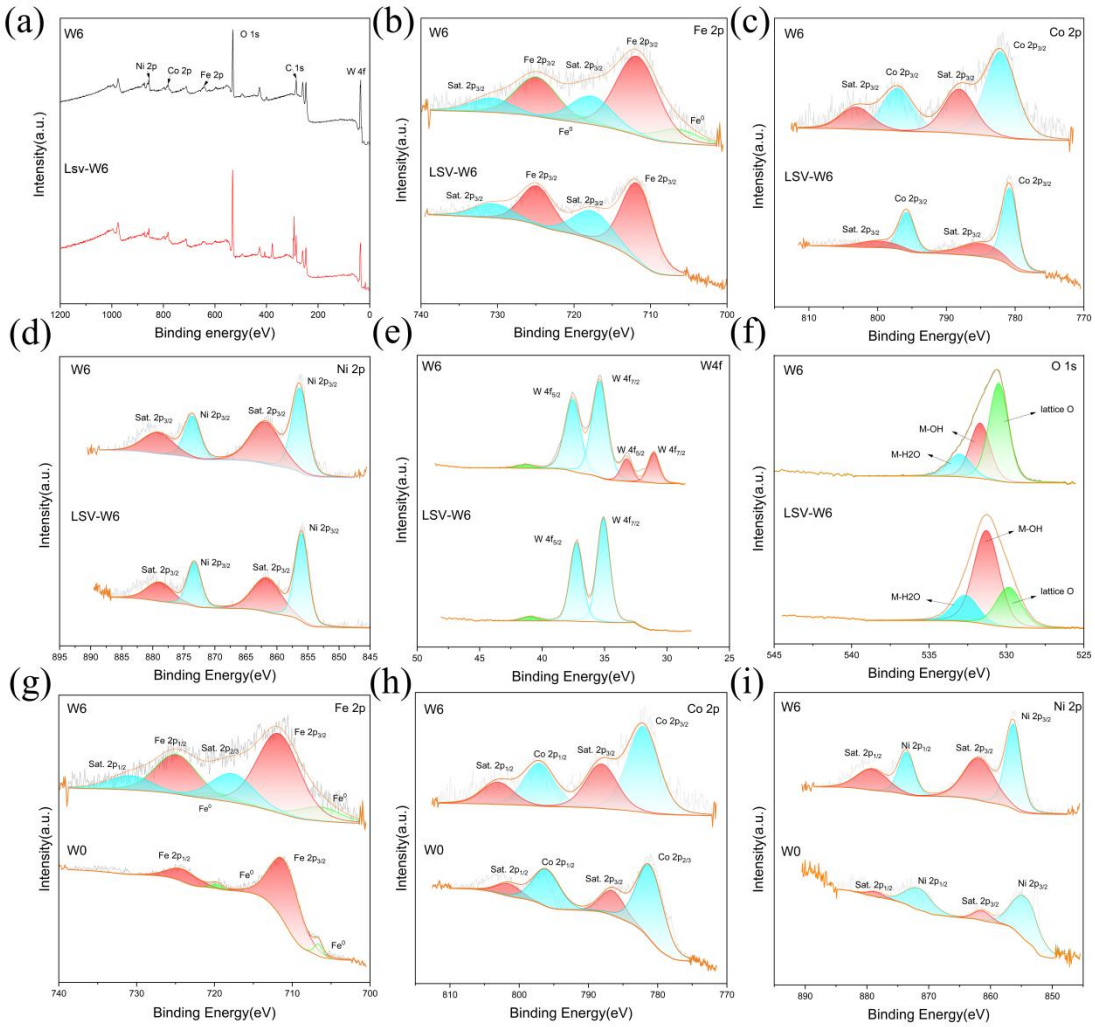

Figure 4. (a) Survey spectra of W6 and LSV-W6; (b)-(f) The high-resolution XPS spectra of Fe 2p, Co 2p, Ni 2p, W 4f, and O 1 s are presented in W6 and LSV-W6; (g)-(i) The high-resolution XPS spectra of Fe 2p, Co 2p, Ni 2p in W6 and W0.

The electrocatalytic OER performance of $FeCoNiW_x$ thin-film catalysts with

varying W content were systematically evaluated using a standard three-electrode configuration. Fig.5(a) shows that LSV measurements were conducted over 8 cycles for W0-W7 electrodes to ensure stable oxide layer formation. Figure.5(b) presents the LSV8 curves of the W0 and FeCoNiW films with different W contents (W2/W4/W6/W7). It can be intuitively observed that at different current densities, the overpotential of the W2/W4/W6/W7 thin films are lower than those of the W0 thin film. As shown in Fig.5(c), the overpotential of W0/W2/W4/W6/W7/NF at a current density of 10 mA cm^{-2} are 303 mV, 296 mV, 283 mV, 264 mV, 270 mV and 355mV, respectively. The overpotential first decreases and then increases with the doping of W content, among which the W6 has the lowest overpotential of 264 mV, indicating that W6 has the best catalytic performance. This value is much lower than FeCoNiCrMo (269 mV)[58], FeCoNiCrMn (282 mV)[59], and FeCoNiMo (364 mV)[60] and. The Tafel slopes calculated from LSV curves are displayed in Fig.5(d). It can be observed that the Tafel slope first decreases and then increases with the increase of W content, and W6 has the smallest Tafel slope (59.09 mV dec^{-1}), indicating the best electrochemical reaction kinetics. It is well-established that a larger electrochemical active surface area (ECSA) correlates with increased density of active sites and enhanced electrocatalytic OER performance[61,62]. The ECSA can be quantitatively determined through the linear proportionality between the electrochemical double-layer capacitance (C_{dl}) and scan rate (v). Fig.5(e) shows the C_{dl} (electrochemical double-layer capacitance) values of W0/W2/W4/W6/W7. It can be observed that the W6 sample exhibits the largest C_{dl} value, indicating that W6 possesses the largest ECSA and more active sites. This finding is consistent with the results of SEM analysis. The chronopotentiometric test (Fig. 5(f)) shows that at a current density of 10 mA cm^{-2}, the potential of NF15CV only increases by 0.11%. This indicates that W6 exhibits excellent stability during the electrocatalytic OER process.

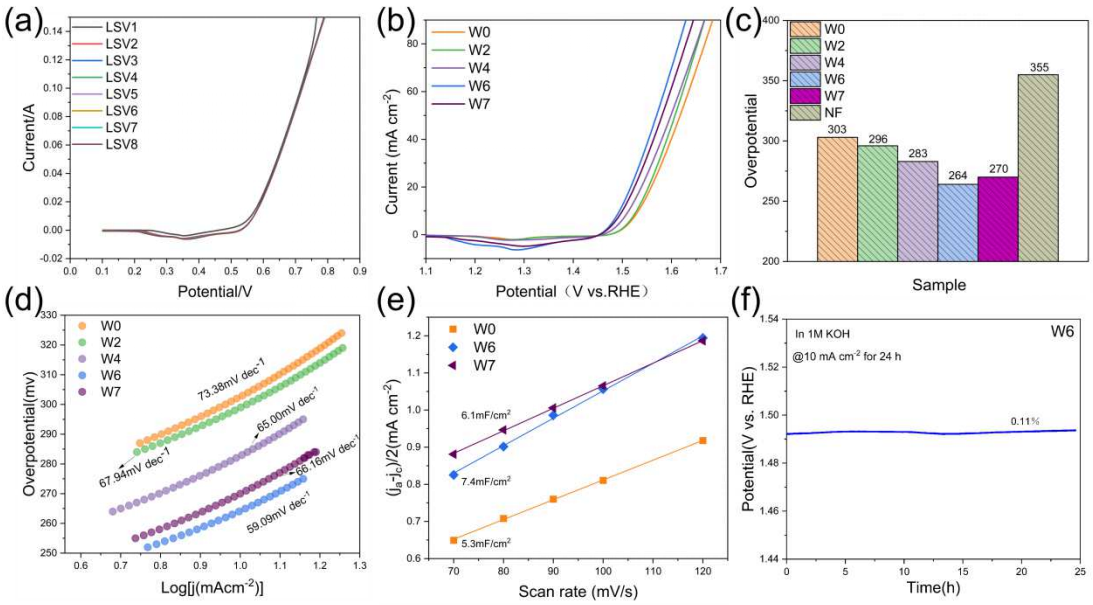

Figure 5. Electrochemical test data of samples with different W content in 1 mol/L KOH. (a) 8 times LSV curves of W6; (b)LSV curves; (c) Overpotential; (d) Tafel plot; (e) Double layer Capacitance at different scan rates; (f) Chronopotentiometric curves of W6 at 10 mA/cm2 for 24 h.

Fig. 6 presents the total DOS of FeCoNiW and FeCoNi, along with the element PDOS for each constituent element. First-principles calculations reveal that the Ni d-band center in FeCoNiW is −2.368 eV, compared to −3.120 eV in FeCoNi, indicating an upward shift of approximately 0.734 eV upon W incorporation. Within the adsorbate evolution mechanism, first-principles calculations show that the adsorption energy of intermediates on Ni sites in both FeCoNi, FeCoNiMoW and FeCoNiMnMo is significantly lower than that on other elements (Co, Ni, Fe, Mo, W) [34,60,63]; thus, Ni sites are typically regarded as the active centers for intermediate binding. Generally, the d-band center reflects the binding strength between adsorption sites and intermediates, with a higher d-band center (closer to the Fermi level) corresponding to stronger intermediate–adsorbate interactions [64]. In this study, the elevated Ni d-band center in FeCoNiW relative to FeCoNi suggests that W doping enhances the binding of intermediates to Ni sites during the OER process, thereby accelerating the OER kinetics.

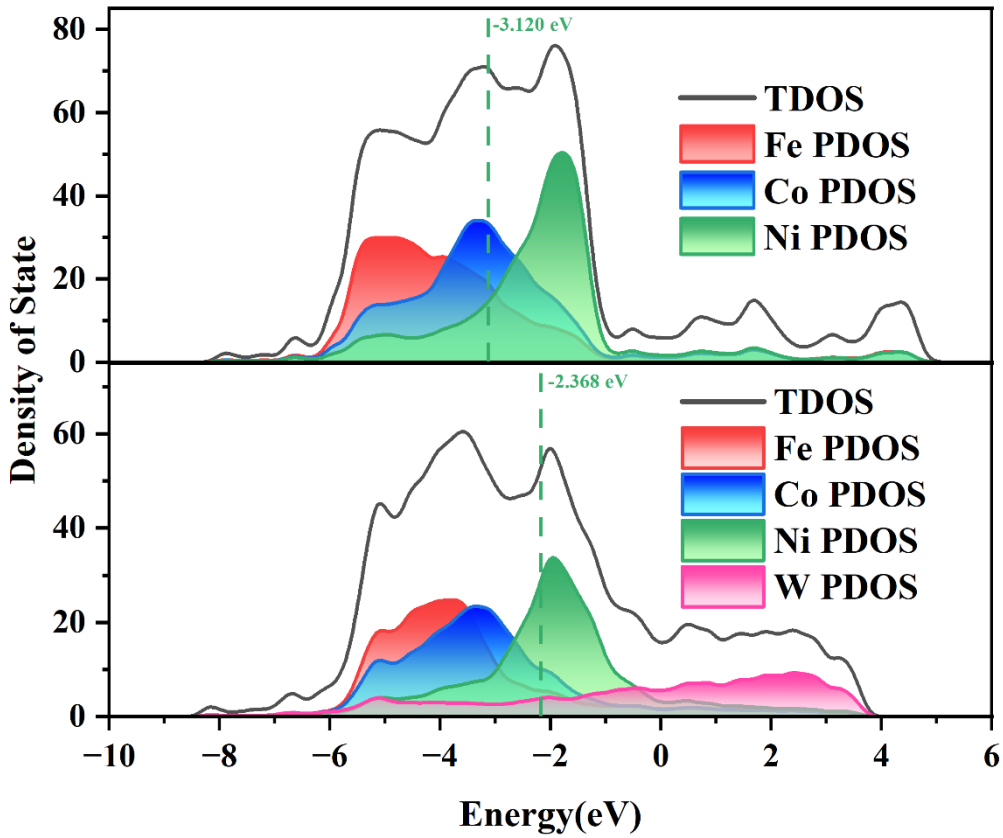

Figure 6. DOS of FeCoNi and FeCoNiW and the PDOS of each element.

4. Conclusion

In summary, medium entropy alloy (FeCoNiW) thin-film electrodes with different W contents were prepared. Through systematic composition engineering of $FeCoNiW_x$ thin films, we demonstrate that W incorporation induces optimization of electronic structure and increasing specific surface area. The overpotential for OER first decreases with the increase in the number of W targets, reaching its minimum when the number of W targets is six. However, as the number of W targets increases further, the overpotential begins to rise. The optimal W6 catalyst (Fe:Co:Ni:W ≈ 1:1:1:5) achieves a low OER overpotential of 264 mV at 10 mA cm^{-2} and a Tafel slope of 59.09 $mVdec^{-1}$, outperforming undoped FeCoNi (303 mV). This performance enhancement may originate from W-induced lattice distortion, the generation of

high-valence Fe oxyhydroxides, and the incorporation of W elements, which elevates the d-band center of Ni. This work provides experimental evidence for the compositional design of catalysts, confirming the critical role of W in regulating OER performance. The findings offer new insights for developing efficient and stable electrocatalysts for water splitting and other energy conversion applications.

References

[1] S. Chu, Y. Cui, N. Liu, The path towards sustainable energy, Nat. Mater. 16 (2017) 16–22. https://doi.org/10.1038/nmat4834.

[2] 05/01470 On hydrogen and hydrogen energy strategies I: Current status and needs, Fuel Energy Abstr. 46 (2005) 222. https://doi.org/10.1016/S0140-6701(05)81477-8.

[3] X. Li, L. Zhao, J. Yu, X. Liu, X. Zhang, H. Liu, W. Zhou, Water Splitting: From Electrode to Green Energy System, Nano-Micro Lett. 12 (2020) 131. https://doi.org/10.1007/s40820-020-00469-3.

[4] R. Cai, M. Ju, J. Chen, J. Ren, J. Yu, X. Long, S. Yang, Recent advances in surface/interface engineering of noble-metal free catalysts for energy conversion reactions, Mater. Chem. Front. 5 (2021) 3576–3592. https://doi.org/10.1039/D1QM00161B.

[5] A. Ali, F. Long, P.K. Shen, Innovative Strategies for Overall Water Splitting Using Nanostructured Transition Metal Electrocatalysts, Electrochem. Energy Rev. 5 (2022) 1. https://doi.org/10.1007/s41918-022-00136-8.

[6] I. Roger, M.A. Shipman, M.D. Symes, Earth-abundant catalysts for electrochemical and photoelectrochemical water splitting, Nat. Rev. Chem. 1 (2017) 0003. https://doi.org/10.1038/s41570-016-0003.

[7] A.M. Oliveira, R.R. Beswick, Y. Yan, A green hydrogen economy for a renewable energy society, Curr. Opin. Chem. Eng. 33 (2021) 100701. https://doi.org/10.1016/j.coche.2021.100701.

[8] H. Wu, Q. Huang, Y. Shi, J. Chang, S. Lu, Electrocatalytic water splitting: Mechanism and electrocatalyst design, Nano Res. 16 (2023) 9142–9157. https://doi.org/10.1007/s12274-023-5502-8.

[9] C. Hu, L. Zhang, J. Gong, Recent progress made in the mechanism comprehension and design of electrocatalysts for alkaline water splitting, Energy Environ. Sci. 12 (2019) 2620–2645. https://doi.org/10.1039/C9EE01202H.

[10] S. Ardizzone, C.L. Bianchi, G. Cappelletti, M. Ionita, A. Minguzzi, S. Rondinini, A. Vertova, Composite ternary SnO2–IrO2–Ta2O5 oxide electrocatalysts, J. Electroanal. Chem. 589 (2006) 160–166. https://doi.org/10.1016/j.jelechem.2006.02.004.

[11] G. Chen, X. Chen, P.L. Yue, Electrochemical Behavior of Novel Ti/IrO$_x$ −Sb_2 O_5 −SnO_2 Anodes, J. Phys. Chem. B 106 (2002) 4364–4369. https://doi.org/10.1021/jp013547o.

[12] J. Cheng, H. Zhang, G. Chen, Y. Zhang, Study of IrxRu1−xO2 oxides as anodic electrocatalysts for solid polymer electrolyte water electrolysis, Electrochimica Acta 54 (2009) 6250–6256. https://doi.org/10.1016/j.electacta.2009.05.090.

[13] K. Kadakia, M.K. Datta, O.I. Velikokhatnyi, P. Jampani, S.K. Park,

S.J. Chung, P.N. Kumta, High performance fluorine doped (Sn,Ru)O2 oxygen evolution reaction electro-catalysts for proton exchange membrane based water electrolysis, J. Power Sources 245 (2014) 362–370. https://doi.org/10.1016/j.jpowsour.2013.06.099.

[14] D.A. Corrigan, ChemInform Abstract: Catalysis of the Oxygen Evolution Reaction by Iron Impurities in Thin Film Nickel Oxide Electrodes., ChemInform 18 (1987) chin.198722015. https://doi.org/10.1002/chin.198722015.

[15] M.W. Louie, A.T. Bell, An Investigation of Thin-Film Ni–Fe Oxide Catalysts for the Electrochemical Evolution of Oxygen, J. Am. Chem. Soc. 135 (2013) 12329–12337. https://doi.org/10.1021/ja405351s.

[16] L. Trotochaud, S.L. Young, J.K. Ranney, S.W. Boettcher, Nickel–Iron Oxyhydroxide Oxygen-Evolution Electrocatalysts: The Role of Intentional and Incidental Iron Incorporation, J. Am. Chem. Soc. 136 (2014) 6744–6753. https://doi.org/10.1021/ja502379c.

[17] J.M.P. Martirez, E.A. Carter, Unraveling Oxygen Evolution on Iron-Doped β-Nickel Oxyhydroxide: The Key Role of Highly Active Molecular-like Sites, J. Am. Chem. Soc. 141 (2019) 693–705. https://doi.org/10.1021/jacs.8b12386.

[18] K. Liu, C. Zhang, Y. Sun, G. Zhang, X. Shen, F. Zou, H. Zhang, Z. Wu, E.C. Wegener, C.J. Taubert, J.T. Miller, Z. Peng, Y. Zhu, High-Performance Transition Metal Phosphide Alloy Catalyst for Oxygen Evolution Reaction, ACS Nano 12 (2018) 158–167. https://doi.org/10.1021/acsnano.7b04646.

[19] L. Han, X. Yu, X.W. (David) Lou, Formation of Prussian-Blue-Analog Nanocages via a Direct Etching Method and their Conversion into Ni–Co-Mixed Oxide for Enhanced Oxygen Evolution, Adv. Mater. 28 (2016) 4601–4605. https://doi.org/10.1002/adma.201506315.

[20] D. Friebel, M.W. Louie, M. Bajdich, K.E. Sanwald, Y. Cai, A.M. Wise, M.-J. Cheng, D. Sokaras, T.-C. Weng, R. Alonso-Mori, R.C. Davis, J.R. Bargar, J.K. Nørskov, A. Nilsson, A.T. Bell, Identification of Highly Active Fe Sites in (Ni,Fe)OOH for Electrocatalytic Water Splitting, J. Am. Chem. Soc. 137 (2015) 1305–1313. https://doi.org/10.1021/ja511559d.

[21] F.-T. Tsai, Y.-T. Deng, C.-W. Pao, J.-L. Chen, J.-F. Lee, K.-T. Lai, W.-F. Liaw, The HER/OER mechanistic study of an FeCoNi-based electrocatalyst for alkaline water splitting, J. Mater. Chem. A 8 (2020) 9939–9950. https://doi.org/10.1039/D0TA01877E.

[22] C. Liang, P. Zou, A. Nairan, Y. Zhang, J. Liu, K. Liu, S. Hu, F. Kang, H.J. Fan, C. Yang, Exceptional performance of hierarchical Ni–Fe oxyhydroxide@NiFe alloy nanowire array electrocatalysts for large current density water splitting, Energy Environ. Sci. 13 (2020) 86–95. https://doi.org/10.1039/C9EE02388G.

[23] J. Hou, Y. Wu, B. Zhang, S. Cao, Z. Li, L. Sun, Rational Design of Nanoarray Architectures for Electrocatalytic Water Splitting, Adv. Funct. Mater. 29 (2019) 1808367. https://doi.org/10.1002/adfm.201808367.

[24] J. -W. Yeh, S. -K. Chen, S. -J. Lin, J. -Y. Gan, T. -S. Chin, T. -T. Shun, C. -H. Tsau, S. -Y. Chang, Nanostructured High-Entropy Alloys with Multiple Principal Elements: Novel Alloy Design Concepts and Outcomes, Adv. Eng. Mater. 6 (2004) 299–303. https://doi.org/10.1002/adem.200300567.

[25] N. Kumar Katiyar, K. Biswas, J.-W. Yeh, S. Sharma, C. Sekhar Tiwary, A perspective on the catalysis using the high entropy alloys, Nano Energy 88 (2021) 106261. https://doi.org/10.1016/j.nanoen.2021.106261.

[26] K. Li, W. Chen, Recent progress in high-entropy alloys for catalysts: synthesis, applications, and prospects, Mater. Today Energy 20 (2021) 100638. https://doi.org/10.1016/j.mtener.2021.100638.

[27] K. Zeng, J. Zhang, W. Gao, L. Wu, H. Liu, J. Gao, Z. Li, J. Zhou, T. Li, Z. Liang, B. Xu, Y. Yao, Surface-Decorated High-Entropy Alloy Catalysts with Significantly Boosted Activity and Stability, Adv. Funct. Mater. 32 (2022) 2204643. https://doi.org/10.1002/adfm.202204643.

[28] T.A.A. Batchelor, J.K. Pedersen, S.H. Winther, I.E. Castelli, K.W. Jacobsen, J. Rossmeisl, High-Entropy Alloys as a Discovery Platform for Electrocatalysis, Joule 3 (2019) 834–845. https://doi.org/10.1016/j.joule.2018.12.015.

[29] S. Wang, B. Xu, W. Huo, H. Feng, X. Zhou, F. Fang, Z. Xie, J.K. Shang, J. Jiang, Efficient FeCoNiCuPd thin-film electrocatalyst for alkaline oxygen and hydrogen evolution reactions, Appl. Catal. B Environ. 313 (2022) 121472. https://doi.org/10.1016/j.apcatb.2022.121472.

[30] Y. Mei, Y. Feng, C. Zhang, Y. Zhang, Q. Qi, J. Hu, High-Entropy Alloy with Mo-Coordination as Efficient Electrocatalyst for Oxygen Evolution Reaction, ACS Catal. 12 (2022) 10808–10817. https://doi.org/10.1021/acscatal.2c02604.

[31] P. Yang, Z. Jiang, Y. Shi, W. Zhang, X. Ren, L. Liang, M. Wang, K. Zhu, Construction of high-entropy oxy/hydroxides with dense nanosheet array structures on FeCoNiCrMo electrode for efficient oxygen evolution reaction, Appl. Phys. Lett. 123 (2023) 091602. https://doi.org/10.1063/5.0161844.

[32] W. Dai, X. Yang, F. Hu, W. Cao, C. Zhao, Y. Zhang, S. Huang, Solution combustion synthesis of hierarchical porous CoNiFeCu0.1 medium-entropy alloy: A highly efficient and robust electrocatalyst for water oxidation, J. Alloys Compd. 952 (2023) 169987. https://doi.org/10.1016/j.jallcom.2023.169987.

[33] H. Park, J.W. Bae, T.H. Lee, I.J. Park, C. Kim, M.G. Lee, S.A. Lee, J.W. Yang, M. Choi, S.H. Hong, S.Y. Kim, S.H. Ahn, J.Y. Kim, H.S. Kim, H.W. Jang, Surface-Tailored Medium Entropy Alloys as Radically Low Overpotential Oxygen Evolution Electrocatalysts, Small 18 (2022) 2105611. https://doi.org/10.1002/smll.202105611.

[34] H. Liu, H. Qin, J. Kang, L. Ma, G. Chen, Q. Huang, Z. Zhang, E. Liu, H. Lu, J. Li, N. Zhao, A freestanding nanoporous NiCoFeMoMn high-entropy alloy as an efficient electrocatalyst for rapid water splitting, Chem. Eng. J. 435 (2022) 134898. https://doi.org/10.1016/j.cej.2022.134898.

[35] S.-Q. Chang, C.-C. Cheng, P.-Y. Cheng, C.-L. Huang, S.-Y. Lu, Pulse electrodeposited FeCoNiMnW high entropy alloys as efficient and stable bifunctional electrocatalysts for acidic water splitting, Chem. Eng. J. 446 (2022) 137452. https://doi.org/10.1016/j.cej.2022.137452.

[36] Z.-L. Wang, G.-Y. Huang, G.-R. Zhu, H.-C. Hu, C. Li, X.-H. Guan, H.-B. Zhu, La-exacerbated lattice distortion of high entropy alloys for enhanced electrocatalytic water splitting, Appl. Catal. B Environ. Energy 361 (2025) 124585. https://doi.org/10.1016/j.apcatb.2024.124585.

[37] W. Dai, T. Lu, Y. Pan, Novel and promising electrocatalyst for oxygen evolution reaction based on MnFeCoNi high entropy alloy, J. Power Sources 430 (2019) 104–111. https://doi.org/10.1016/j.jpowsour.2019.05.030.

[38] M. Luo, S. Guo, Strain-controlled electrocatalysis on multimetallic nanomaterials, Nat. Rev. Mater. 2 (2017) 17059. https://doi.org/10.1038/natrevmats.2017.59.

[39] S. Bhattacharjee, U.V. Waghmare, S.-C. Lee, An improved d-band model of the catalytic activity of magnetic transition metal surfaces, Sci. Rep. 6 (2016) 35916. https://doi.org/10.1038/srep35916.

[40] R. He, L. Yang, Y. Zhang, D. Jiang, S. Lee, S. Horta, Z. Liang, X. Lu, A. Ostovari Moghaddam, J. Li, M. Ibáñez, Y. Xu, Y. Zhou, A. Cabot, A 3d-4d-5d High Entropy Alloy as a Bifunctional Oxygen Catalyst for Robust Aqueous Zinc–Air Batteries, Adv. Mater. 35 (2023) 2303719. https://doi.org/10.1002/adma.202303719.

[41] B.J. Kim, J. Yu, H. Koh, I. Nagai, S.I. Ikeda, S.-J. Oh, C. Kim, Missing x y -Band Fermi Surface in 4 d Transition-Metal Oxide Sr 2 RhO 4 : Effect of the Octahedra Rotation on the Electronic Structure, Phys. Rev. Lett. 97 (2006) 106401. https://doi.org/10.1103/PhysRevLett.97.106401.

[42] Y. Ye, H. Zhang, X. Cao, Z. Zhang, X. Zuo, Q. Yang, H. Tang, S. Jin, G. Li, FeCoNiW medium entropy alloys loaded onto N-doped carbon skeletons as efficient electrocatalysts for oxygen evolution reactions, New J. Chem. 48 (2024) 5797–5803. https://doi.org/10.1039/D4NJ00011K.

[43] J. Yan, L. Kong, Y. Ji, J. White, Y. Li, J. Zhang, P. An, S. Liu, S.-T. Lee, T. Ma, Single atom tungsten doped ultrathin α-Ni(OH)2 for enhanced electrocatalytic water oxidation, Nat. Commun. 10 (2019) 2149. https://doi.org/10.1038/s41467-019-09845-z.

[44] T. Zhang, H.-F. Zhao, Z.-J. Chen, Q. Yang, N. Gao, L. Li, N. Luo, J. Zheng, S.-D. Bao, J. Peng, X. Peng, X.-W. Liu, H.-B. Yu, High-entropy alloy enables multi-path electron synergism and lattice oxygen activation for enhanced oxygen evolution activity, Nat. Commun. 16 (2025) 3327. https://doi.org/10.1038/s41467-025-58648-y.

[45] A.T. Bell, The Impact of Nanoscience on Heterogeneous Catalysis, Science 299 (2003) 1688–1691. https://doi.org/10.1126/science.1083671.

[46] J.P. Perdew, K. Burke, M. Ernzerhof, Generalized Gradient Approximation Made Simple [Phys. Rev. Lett. 77, 3865 (1996)], Phys. Rev. Lett. 78 (1997) 1396–1396. https://doi.org/10.1103/PhysRevLett.78.1396.

[47] J.P. Perdew, M. Ernzerhof, K. Burke, Rationale for mixing exact exchange with density functional approximations, J. Chem. Phys. 105 (1996) 9982–9985. https://doi.org/10.1063/1.472933.

[48] F. Rehman, M. Delowar Hossain, A. Tyagi, D. Lu, B. Yuan, Z. Luo, Engineering electrocatalyst for low-temperature N2 reduction to ammonia, Mater. Today 44 (2021) 136–167. https://doi.org/10.1016/j.mattod.2020.09.006.

[49] Y. Chen, M. Wang, S. Xiang, J. Liu, S. Feng, C. Wang, N. Zhang, T. Feng, M. Yang, K. Zhang, B. Yang, Hierarchical Hollow Nanocages Derived from Polymer/Cobalt Complexes for Electrochemical Overall Water Splitting, ACS Sustain. Chem. Eng. 7 (2019) 10912–10919. https://doi.org/10.1021/acssuschemeng.9b01789.

[50] M.C. Biesinger, B.P. Payne, A.P. Grosvenor, L.W.M. Lau, A.R. Gerson, R.St.C. Smart, Resolving surface chemical states in XPS analysis of first row transition metals, oxides and hydroxides: Cr, Mn, Fe, Co and Ni, Appl. Surf. Sci. 257 (2011) 2717–2730. https://doi.org/10.1016/j.apsusc.2010.10.051.

[51] L. Hu, J. Shi, Z. Peng, Z. Zheng, H. Dong, T. Wang, A high-density nickel–cobalt alloy embedded in nitrogen-doped carbon nanosheets for the hydrogen evolution reaction, Nanoscale 14 (2022) 6202–6211. https://doi.org/10.1039/D2NR00053A.

[52] J. Dong, Y. Wang, Q. Jiang, Z.-A. Nan, F.R. Fan, Z.-Q. Tian, Charged droplet-driven fast formation of nickel–iron (oxy)hydroxides with rich oxygen defects for boosting overall water splitting, J. Mater. Chem. A 9 (2021) 20058–20067. https://doi.org/10.1039/D1TA05332A.

[53] X. Bo, R.K. Hocking, S. Zhou, Y. Li, X. Chen, J. Zhuang, Y. Du, C. Zhao, Capturing the active sites of multimetallic (oxy)hydroxides for the oxygen evolution reaction, Energy Environ. Sci. 13 (2020) 4225–4237. https://doi.org/10.1039/D0EE01609H.

[54] G. Fu, W. Li, J. Zhang, M. Li, C. Li, N. Li, Q. He, S. Xi, D. Qi, J.L. MacManus-Driscoll, J. Cheng, K.H. Zhang, Facilitating the Deprotonation of OH to O through Fe^{4+} -Induced States in Perovskite $LaNiO_3$ Enables a Fast Oxygen Evolution Reaction, Small 17 (2021) 2006930. https://doi.org/10.1002/smll.202006930.

[55] K.T. Ng, D.M. Hercules, Studies of nickel-tungsten-alumina catalysts by x-ray photoelectron spectroscopy, J. Phys. Chem. 80 (1976) 2094–2102. https://doi.org/10.1021/j100560a009.

[56] S. Wang, B. Xu, W. Huo, H. Feng, X. Zhou, F. Fang, Z. Xie, J.K. Shang, J. Jiang, Efficient FeCoNiCuPd thin-film electrocatalyst for alkaline oxygen and hydrogen evolution reactions, Appl. Catal. B Environ. 313 (2022) 121472. https://doi.org/10.1016/j.apcatb.2022.121472.

[57] S. Wang, W. Huo, F. Fang, Z. Xie, J.K. Shang, J. Jiang, High entropy alloy/C nanoparticles derived from polymetallic MOF as promising electrocatalysts for alkaline oxygen evolution reaction, Chem. Eng. J. 429 (2022) 132410. https://doi.org/10.1016/j.cej.2021.132410.

[58] P. Yang, Y. Liu, K. Zhu, Effect of Mo on surface reconstruction of

FeCoNi-based high entropy alloy film electrode for oxygen evolution reaction, Surf. Coat. Technol. 494 (2024) 131392. https://doi.org/10.1016/j.surfcoat.2024.131392.

[59] P. Yang, Y. Shi, T. Xia, Z. Jiang, X. Ren, L. Liang, Q. Shao, K. Zhu, Novel self-supporting thin film electrodes of FeCoNiCrMn high entropy alloy for excellent oxygen evolution reaction, J. Alloys Compd. 938 (2023) 168582. https://doi.org/10.1016/j.jallcom.2022.168582.

[60] R. He, L. Yang, Y. Zhang, D. Jiang, S. Lee, S. Horta, Z. Liang, X. Lu, A. Ostovari Moghaddam, J. Li, M. Ibáñez, Y. Xu, Y. Zhou, A. Cabot, A 3d-4d-5d High Entropy Alloy as a Bifunctional Oxygen Catalyst for Robust Aqueous Zinc–Air Batteries, Adv. Mater. 35 (2023) 2303719. https://doi.org/10.1002/adma.202303719.

[61] X. Hu, S. Zhang, J. Sun, L. Yu, X. Qian, R. Hu, Y. Wang, H. Zhao, J. Zhu, 2D Fe-containing cobalt phosphide/cobalt oxide lateral heterostructure with enhanced activity for oxygen evolution reaction, Nano Energy 56 (2019) 109–117. https://doi.org/10.1016/j.nanoen.2018.11.047.

[62] J. Zhou, L. Yuan, J. Wang, L. Song, Y. You, R. Zhou, J. Zhang, J. Xu, Combinational modulations of $NiSe_2$ nanodendrites by phase engineering and iron-doping towards an efficient oxygen evolution reaction, J. Mater. Chem. A 8 (2020) 8113–8120. https://doi.org/10.1039/D0TA00860E.

[63] H. Zhao, J. Yao, Y. Wang, N. Gao, T. Zhang, L. Li, Y. Liu, Z. Chen, J. Peng, X. Liu, H. Yu, Crystal Facets-Activity Correlation for Oxygen Evolution Reaction in Compositional Complex Alloys, Adv. Sci. 11 (2024) 2404095. https://doi.org/10.1002/advs.202404095.

[64] E. Santos, W. Schmickler, d-Band Catalysis in Electrochemistry, ChemPhysChem 7 (2006) 2282–2285. https://doi.org/10.1002/cphc.200600441.